Earth Planet. Sci. Lett. 650 (2025) 119116

Contents lists available at ScienceDirect

Earth and Planetary Science Letters

journal homepage: www.elsevier.com/locate/epsl

Ocean crustal veins record dynamic interplay between plate-cooling-induced cracking and ocean chemistry

Aled D. Evans [a,*], Rosalind M. Coggon [a], Michelle Harris [b], Elliot J. Carter [c], Elmar Albers [d], Gilles M. Guérin [e], Thomas M. Belgrano [f], Mallika Jonnalagadda [g], Lewis J.C. Grant [a], Pamela D. Kempton [h], David J. Sanderson [a], James A. Milton [a], Timothy J. Henstock [a], Jeff C. Alt [i], Damon A.H. Teagle [a]

[a] School of Ocean and Earth Science, National Oceanography Centre Southampton, University of Southampton, Southampton, SO14 3ZH, UK
[b] School of Geography, Earth and Environmental Sciences, University of Plymouth, Plymouth, PL4 8AA, UK
[c] School of Life Sciences, Keele University, Staffordshire, ST5 5BG, UK
[d] Department of Geology & Geophysics, Woods Hole Oceanographic Institution, Woods Hole, MA 02543, USA
[e] Lamont Doherty Earth Observatory, Columbia University, NY, USA
[f] UCD School of Earth Sciences, University College Dublin, Dublin, Ireland
[g] Interdisciplinary School of Science, Savitribai Phule Pune University, Pune, India
[h] Department of Geology, Kansas State University, Manhattan, KS, USA
[i] Department of Earth and Environmental Science, University of Michigan, Ann Arbor, Michigan 48109, USA

ARTICLE INFO

Keywords:
Ocean crust alteration
carbon cycle
plate cooling
ocean chemistry
hydrothermal veins
thermal contraction

ABSTRACT

As ocean crust traverses away from spreading ridges, low-temperature hydrothermal minerals fill cracks to form veins, transforming the physical and chemical properties of ocean crust whilst also modifying the composition of seawater. Vein width and frequency observations compiled from the International Ocean Discovery Program (IODP) South Atlantic Transect (~31°S) and previous scientific ocean drilling holes show that vein width distributions progressively broaden and observed strain ($\Sigma m_{veins}/m_{core}$) increases with crustal age, whereas vein densities ($\#_{veins}/m_{core}$) remain approximately constant. Elemental mapping and textural observations illuminate multiple precipitation and fracturing episodes that continue as the ocean crust ages. This challenges the existing notion that ocean crustal veins are passively filled; rather, they are dynamic features of ocean crust aging. These data, combined with thermal strain modelling, indicate a positive feedback mechanism where cooling of the ocean plate induces cracking and the reactivation of pre-existing veins, ultimately resulting in further cooling. Waning of this feedback provides a mechanism for the termination of the global average heat flow anomaly. Sites with total vein dilation greater than expected for their age correspond with crustal formation during periods of high atmospheric CO_2. The amount of vein material thus reflects the changing balance between ocean plate cooling, ocean chemistry, and the age of the ocean crust. Our results demonstrate that ocean crust endures as an active geochemical reservoir for tens of millions of years after formation.

1. Introduction

Interactions between cooling ocean crust and seawater-derived fluids influence the planetary recycling of materials between Earth's surficial envelopes and interior, as well as seawater chemistry, biogeochemical cycles, and climate (Alt and Teagle, 1999; Coggon et al., 2016, 2016). These hydrothermal exchanges are manifest by the precipitation of secondary minerals that partially to completely replace primary minerals, and fill open spaces through which fluids circulate, including fractures to form veins. These veins provide robust records of the conditions of fluid-rock exchange (Alt and Teagle, 2003; Coggon et al., 2004, 2016). Yet, how the physical and chemical characteristics of upper crustal veins evolve in space and time remains poorly constrained. Previous quantification of veins in ocean crust indicate that crust formed in the Mesozoic (Fig. 1) has significantly greater vein volumetric abundance, in particular of carbonate veins, than younger crustal

* Corresponding author.
E-mail address: A.Evans@soton.ac.uk (A.D. Evans).

https://doi.org/10.1016/j.epsl.2024.119116
Received 19 June 2024; Received in revised form 8 November 2024; Accepted 12 November 2024
Available online 22 November 2024

sections (Alt and Teagle, 1999). However, whether increasing vein material abundance with crustal age is related to the progressive aging of ocean crust or different ocean chemistry at the time of crustal formation remains unresolved (Alt and Teagle, 1999; Gillis and Coogan, 2011). Establishing the dominance of these differing drivers is key to quantifying the contribution of the low temperature alteration of the ocean crust to global biogeochemical cycles (Berner et al., 1983; Berner and Berner, 1997). Radiometric dating of the formation age of secondary minerals remains technically challenging (Albers et al., 2023; Coogan et al., 2016; Kendrick et al., 2022), and not all vein types can be dated. Age determinations of calcium carbonate and celadonite indicate formation over prolonged time periods up to 60 million years, albeit with most precipitation occurring within ~30 Myr of crustal formation (Fig. 2c) (Coogan et al., 2016; Hart and Staudigel, 1986; Kendrick et al., 2022; Laureijs et al., 2021). These ages, from veins distributed throughout each drill hole, indicate prolonged fluid flow is widely distributed through an upper ocean crustal crack network.

Despite a wide range of spreading rates, lava morphologies, crustal architectures, sediment thicknesses and differing extents of volcanic basement exposed directly on the seafloor, hydrothermal advective heat loss requiring hydrothermal fluid flow is discernible globally on average in crust 65 ± 10 Ma, after which the ocean crust is considered thermally 'sealed' (Fig. 2a) (Stein and Stein, 1994). The cementation of ocean crust through the filling of fractures by hydrothermal minerals leading to the restriction of the circulation of seawater-derived fluids is a commonly inferred mechanism for the decrease with age of the discrepancy between observed and modelled conductive heat flow (Fig. 2a) (Anderson et al., 1977; Stein and Stein, 1994, 1992). However, rapidly increasing

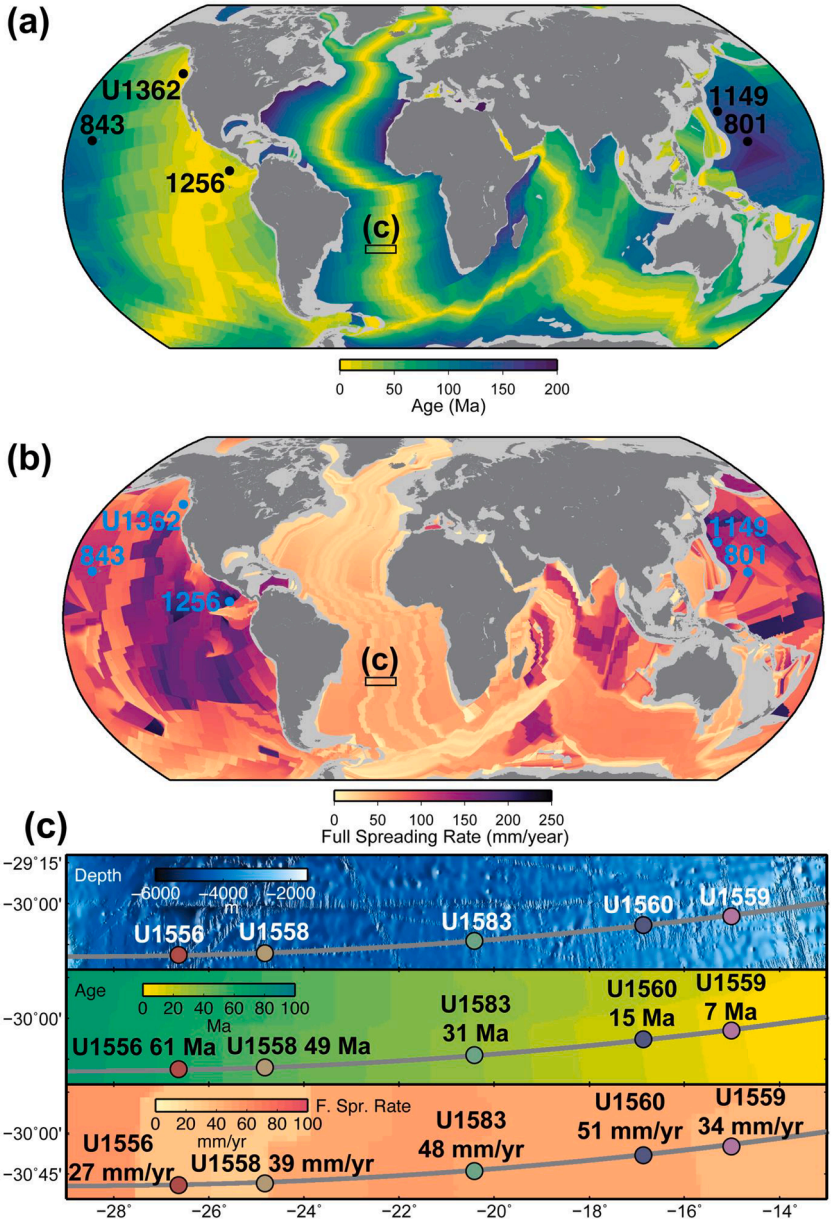

Fig. 1. (a) Map of the present-day age of ocean crust (Seton et al., 2020). Previous scientific ocean drilling sites are shown in black. (b) Map of present-day variations in full spreading rates (mm/yr) (Seton et al., 2020). Previous scientific ocean drilling sites are shown in blue. (c) Inset map of the ~30°S western flank of the south Atlantic showing regional bathymetry (Ryan et al., 2009) and globally compiled seafloor age and full spreading rate grids (Seton et al., 2020), with relative differences mapped using a linear colour scale. Sites drilled by the International Ocean Discovery Program (IODP) South Atlantic Transect (Expedition 390C, 395E, 390 and 393) are shown (Coggon et al., 2024) with respective site crustal ages and full spreading rates (Kardell et al., 2019). Grey line shows the CREST seismic reflection profiles (Reece and Estep, 2019).

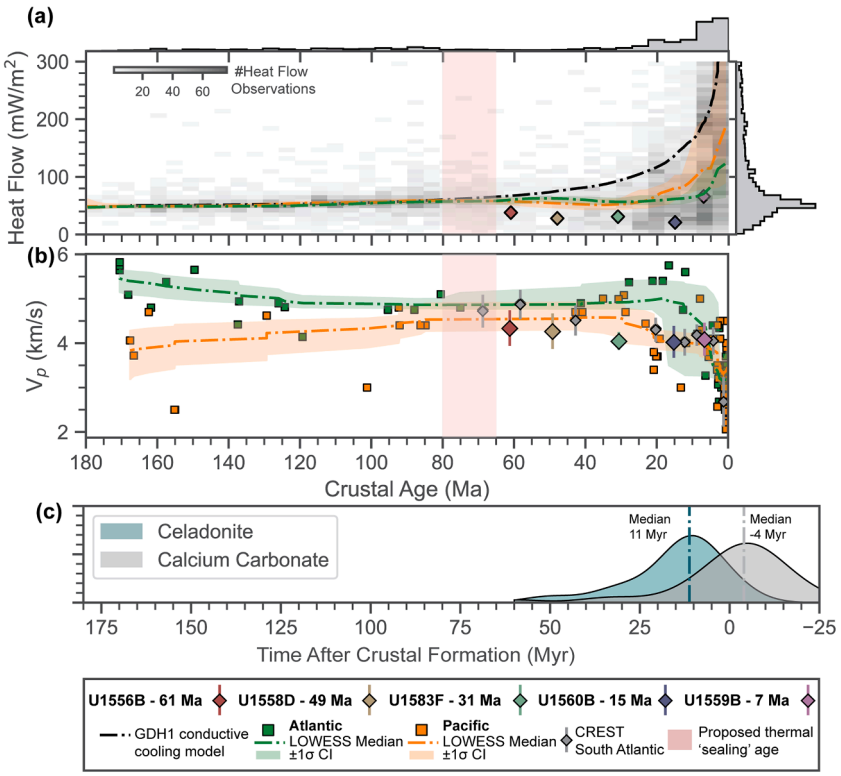

Fig. 2. (a) Two-dimensional density histogram plot of observed heat flow and crustal age from the Pacific and Atlantic with heat flow data compiled from the global dataset of Fuchs et al. (2021). Crustal age is extracted using a seafloor age grid of Seton et al. (2020). Black dashdotted line shows the GDH1 theoretical conductive plate cooling model of Stein and Stein (1992). The difference between measured and expected conductive heat flow is termed the hydrothermal heat flow anomaly and persists for at least 65 to 80 Myr in the Pacific and Atlantic and is shown by pink shading. Heat flow observation intensity is shown by grey shading, colour mapped to a linear greyscale. Green and orange dashdotted lines and corresponding shading reflect median observed heat flow (mW/m^2) values with shaded area equivalent to 1σ. Median values and associated uncertainty were estimated using robust parameter bootstrapped (n=100,000) non-parametric regressions (LOWESS; defined as locally weighted scatter plot smoothing; Cleveland, 1979). (b) P-wave seismic velocities of seismic layer 2A plotted against crustal age with Pacific and Atlantic data compiled from Christeson et al. (2019) and South Atlantic Transect data from Kardell et al. (2019). Data points are plotted as mean values with error bars corresponding to 1σ. Green and orange dashdotted lines and corresponding shading reflect median observed V_p (km/s) values with shaded area equivalent to 1σ. Median values and associated uncertainty were estimated using robust parameter bootstrapped (n=100,000) non-parametric regressions (LOWESS; defined as locally weighted scatter plot smoothing; Cleveland, 1979). (c) Probability density functions of formation of celadonite (Hart and Staudigel, 1986; Laureijs et al., 2021) and calcium carbonate (Coogan et al., 2016; Kendrick et al., 2022) after crustal formation. Ages within respective probability distributions were calculated by subtracting published mean ages from published ages of crustal accretion at respective sites. Dashdotted lines reflect the median values of respective distributions. We note that radiometric dating of calcium carbonate has only occurred in typical basaltic upper ocean crust older than 80 Ma.

upper crustal seismic velocities and sparse in situ measurements that suggest decreasing permeability and interconnected porosity in young ocean crust are both interpreted to result from the filling of open spaces by secondary minerals as the crust ages (Fig. 2b) (Anderson et al., 1977; Christeson et al., 2019; Houtz and Ewing, 1976; Jacobson, 1992; Moos and Marion, 1994; Kardell et al., 2019). The majority of these changes (Carlson, 2014; Fisher and Becker, 2000; Jacobson, 1992; Jarrard et al., 2003; Wilkens et al., 1991) occur within ~8 Myr of crustal formation (Grevemeyer et al., 1999; Jacobson, 1992; Rohr, 1994) suggesting greatly reduced fluid flow and consequent mineral precipitation.

Clearly there is disagreement between heat flow observations and mineral data that suggest hydrothermal circulation is widely distributed in the upper crust for tens of millions of years and seismic data that indicates the upper crust is effectively fully matured by approximately 8 million years. Although previous modelling has postulated that the discrepancy between hydrothermal heat flow and permeability measurements can be explained by lateral channelled flow along narrow horizons (Fisher and Becker, 2000), these zones have yet to be sampled and do not explain the distribution of a wide range of ages of secondary minerals down boreholes. Here, we present observations on the distribution, thickness, and mineralogy of hydrothermal veins from new scientific boreholes drilled into intact in-situ upper ocean crust and integrate these data with published observations (Fig. 1a). The South Atlantic Transect campaign (SAT; International Ocean Discovery Program (IODP) Expeditions 390, 393, 390C, and 395E) drilled a transect across the western flank of the southern Mid-Atlantic Ridge at ~31°S, coring 7, 15, 31, 49, and 61 Ma upper crust that formed at slow to intermediate-spreading rates along a crustal flow line (Fig. 1b) (Coggon et al., 2024a). This transect of holes allows for the first time the systematic investigation of ridge-flank fluid-rock interactions with increasing age over tens of millions of years (Coggon et al., 2024a).

2. Methods

2.1. Core logging

During scientific ocean drilling expeditions that recover basement rocks, veins are systematically logged. The physical characteristic of each vein is logged, such as its depth, length, width, colour, orientation, fill composition, texture, connectivity, and morphology. We compiled vein data from the South Atlantic Transect IODP Expeditions 390 and 393 (Coggon et al., 2024a, 2024b, 2022; Teagle et al., 2023) and previous scientific ocean drilling expeditions (Table 1). Sites were selected for use in the compilation if: (i) intact, in situ, upper basaltic ocean crust was recovered and (ii) each macroscopically visible vein individually logged. As a result, each vein dataset is comparable. All veins were

Table 1
Results summary table of veins logged during the South Atlantic Transect (Coggon et al., 2024) and other expeditions. Data sources: U1362A vein log (Expedition 327 Scientists, 2011), 1256D vein log Leg 206 (Shipboard Scientific Party, 2003), 843B Leg 136 (Shipboard Scientific Party, 1992), 1149D Leg 185 (Shipboard Scientific Party, 2000), 801C Leg 185 (Shipboard Scientific Party, 2000). Full spreading rate classification of Christeson et al. (2019) follows: ultraslow <10 mm/yr, slow 10 to 40 mm/yr, intermediate 40 to 80 mm/yr, fast 80 to 160 mm/yr; superfast >160 mm/yr. Full spreading rate classification of Seton et al. (2020) follows: ultraslow <20 mm/yr, slow >20 to 55 mm/yr, intermediate >55 to 75 mm/yr, fast >75 to 180 mm/yr, superfast >180 mm/yr. We report asymmetric uncertainties equivalent to either 1σ or 2σ respectively.

Hole	U1362A	U1559B	1256D	U1560B	U1583F	U1558D	U1556B	843B	1149D	801C
Age (Ma)	3.6	7	15	15	31	49	61	110	132	167
Full spreading rate (mm/yr)	58	34	220	51	48	39	27	100	102	160
Spreading rate classification (Christeson et al., 2019)	Intermediate	Slow	Superfast	Intermediate	Intermediate	Slow	Slow	Fast	Intermediate/ Fast	Fast
Spreading rate classification (Seton et al., 2020)	Intermediate	Slow	Superfast	Slow	Slow	Slow	Slow	Fast	Intermediate/ Fast	Fast
Ocean plate	Juan de Fuca	South Atlantic	Cocos	South Atlantic	South Atlantic	South Atlantic	South Atlantic	Pacific	Pacific	Pacific
Ocean basin	Pacific	Atlantic	Pacific	Atlantic	Atlantic	Atlantic	Atlantic	Pacific	Pacific	Pacific
Total number of veins	1218	300	3536	2663	1143	2963	5024	362	956	3901
Drilled length (msb)	150	49	300*	192.2	138.5	220.2	342.2	33.7	168.2	341.4†
Recovered core length (m)	44.4	11	158.7*	74.8	45.8	100.8	192	12.2	28.8	160†
Hole recovery (%)	30	26	53*	39	33	46	56	37	17	47†
Number of Cores	20	11	46	39	26	36	58	4	15	40
Range of vein widths (mm)	0.1 to 10	0.1 to 3	0.1 to 15	0.1 to 3.5	0.1 to 7	0.1 to 9	0.1 to 30	0.1 to 10	0.1 to 15	0.1 to 25
Median vein width (mm)	$0.1+^{1}$ (2σ)	$0.2\pm^{1.5}_{0.1}$ (2σ)	$0.2\pm^{1.5}_{0.1}$ (2σ)	$0.1+^{1}$ (2σ)	$0.2\pm^{2}_{0.1}$ (2σ)	$0.2\pm^{2}_{0.1}$ (2σ)	$0.2\pm^{2}_{0.1}$ (2σ)	$0.5\pm^{2.5}_{0.2}$ (2σ)	$0.3\pm^{2}_{0.1}$ (2σ)	$0.3\pm^{4}_{0.1}$ (2σ)
Mean vein width (mm)	0.2	0.4	0.3	0.2	0.4	0.5	0.5	0.8	0.6	0.7
Median vein density (veins/m)	$31\pm^{14}_{17}$ (2σ)	$20\pm^{11}_{4}$ (2σ)	$26\pm^{26}_{20}$ (2σ)	$34\pm^{11}_{14}$ (2σ)	$30\pm^{12}_{15}$ (2σ)	$29\pm^{17}_{8}$ (2σ)	$25\pm^{13}_{16}$ (2σ)	$25\pm^{5}_{4}$ (2σ)	$34\pm^{12}_{11}$ (2σ)	$23\pm^{16}_{10}$ (2σ)
Median Strain (%)	$0.7\pm^{0.5}_{0.4}$ (2σ)	$0.9\pm^{0.7}_{0.5}$ (2σ)	$0.8\pm^{1.2}_{0.6}$ (2σ)	$0.8\pm^{0.4}_{0.4}$ (2σ)	$1\pm^{0.8}_{0.7}$ (2σ)	$1.4\pm^{1.1}_{0.6}$ (2σ)	$1\pm^{1.6}_{0.7}$ (2σ)	$1.8\pm^{1}_{0.9}$ (2σ)	$2\pm^{1}_{0.9}$ (2σ)	$1.3\pm^{1.5}_{1}$ (2σ)
Median value of average vein width per vein per metre core (mm/(veins/m)	$0.4\pm^{0.8}_{0.3}$ (2σ)	$0.4\pm^{0.2}_{0.3}$ (2σ)	$0.8\pm^{3.2}_{0.6}$ (2σ)	$0.3\pm^{0.5}_{0.2}$ (2σ)	$0.4\pm^{1.8}_{0.3}$ (2σ)	$1\pm^{2.7}_{0.8}$ (2σ)	$1.1\pm^{2.8}_{0.8}$ (2σ)	$1.9\pm^{3.8}_{1.5}$ (2σ)	$0.9\pm^{1.5}_{0.7}$ (2σ)	$1.9\pm^{4.3}_{1.8}$ (2σ)
% of multiple event veins	-	62	-	54	64	67	-	-	-	-

* Top 300 m of 1256D only
† Leg 185 vein log only

utilised in the compilation, regardless of morphology, fill composition, and texture. During vein logging, veins are typically binned into widths of 0.1 mm, 0.2 mm, 0.5 mm, 1 mm etc., with 0.5 mm wide bins used for thicker veins. Although the minimum vein width logged is 0.1 mm, the 0.1 width bin includes veins <0.1 mm wide that are still visible in hand-specimen. In younger sites, where veins are on average logged as ~0.1 mm wide (Fig. 4), this vein width bin resolution likely results in an overestimation in the strain (sum of vein widths / recovered length of core; $\frac{\Sigma m_{veins}}{m_{core}}$) of these sites.

Scientific ocean drilling collects cores from vertical boreholes, with recovered cylindrical cores split along a central line into a working half and archive half. Vein logging is undertaken on the cut surface of the archive half of the cores. This cut surface acts as a 1D line transect through the upper ocean crust. Complete core recovery is rare during scientific ocean drilling campaigns that drill basement rocks, ranging between 17 and 56 % on average at the sites studied here (Table 1), and as a result recovered core lengths are variable. Although core recovery is incomplete, no relationship occurs between vein density (number of veins per meters of recovered core; i.e. vein intensity; $\#_{veins}\ /m_{core}$) and recovery of each core (Fig. S1). This suggests that despite incomplete recovery, variations in vein density at, and between, sites are preserved in the recovered material and recorded.

2.2. Elemental mapping

In situ elemental mapping was undertaken at the School of Ocean and Earth Science, National Oceanography Centre Southampton. Sr elemental imaging (at 2 μm x 2 μm pixel resolution) was performed using a Nu Instruments (Nu Instruments Ltd., Wrexham, Wales) Vitesse TOF-ICP mass spectrometer coupled to an Elemental Scientific Lasers (Bozeman, MT, USA) imageGEO193 laser ablation system with a TwoVol3 ablation chamber and Dual Concentric Injector. The instrumental set-up permits fast quasi-simultaneous detection across almost the entire elemental mass range (20–260 m/z). Instrument optimisation was performed while ablating NIST SRM612, a silicate glass reference material, to achieve high sensitivity across the elemental mass whilst minimising oxide production (UO+/U+ <1 %) and laser-induced elemental fractionation (238U+/232Th+ ≈1). Operating conditions are reported in Table S2.

Sr calibration was achieved using bracketed measurements of NIST SRM612 and NIST SRM610. Signal intensity data per sample pixel were exported for data reduction in Iolite 4 using the Trace_Elements data reduction scheme (Paton et al., 2011). Intensities (in cps) were internally normalised to 43Ca based on the expected Ca concentrations in the sample material analysed and the standards. Corrected intensities were subsequently calibrated using a factor derived from repeat analyses of the NIST SRM's. Drift in the Ca and Sr intensities for the reference materials were smoothed with a spline function ("Spline_Smooth 1″) and concentrations reported by Jochum et al. (2005) were used in the calculations. The mapped area was 6 × 2 mm (Fig. S2).

3. Vein evolution in space and time

Hydrothermal veins are ubiquitous features of upper ocean crust (Alt and Teagle, 1999; Coggon et al., 2016). Low temperature (~<80 °C) secondary minerals that precipitate in upper ocean crustal veins include celadonite, iron oxy-hydroxides, magnesium saponite, pyrite, calcium carbonate, and zeolites (Alt et al., 1996). The order of precipitation depends on local geology, although calcium carbonates tend to form relatively late in the alteration sequence (Alt, 2004; Alt et al., 2010; Alt and Teagle, 1999, 2003; Coggon et al., 2024a). Basalt-hosted upper ocean crustal veins are predominantly filled by calcium carbonate and clays (Alt, 2004; Alt et al., 2010; Alt and Teagle, 1999, 2003; Coggon

et al., 2024a) with precipitation typically occurring at temperatures <25 °C (Coggon et al., 2016; Coggon and Teagle, 2011; Coogan and Gillis, 2018) from fluids heated <10 °C above contemporaneous bottom seawater temperatures (Bach and Edwards, 2003), either infilling monomineralic veins or occurring within the same filled crack (Fig. 3). Episodic precipitation of calcium carbonate and clay, with clay commonly forming in the centre of veins suggests temporally distinct fluid pulses associated with low temperature ridge-flank alteration of seafloor basalts.

In addition to recording the composition of the fluids they precipitated from (Coggon et al., 2004), these veins have distinct microstructures that indicate their genesis and subsequent evolution (Bons et al., 2012; Ramsay, 1980) as the ocean crust ages. During the scientific ocean drilling expeditions utilised in this study, the physical characteristics of all recovered macroscopically visible veins (see methods) were systematically and quantitatively recorded during core logging (Table 1). Ocean crustal veins primarily occur as extensional syntaxial vein fills that seal interconnected porosity (Fig. 3). Some, but not all, veins display evidence of multiple precipitation episodes (Alt and Teagle, 1999, 2003; Dilek, 1998; Li et al., 2016; Tartarotti et al., 1996) with several layers of crystals, typically grown perpendicular to the vein wall towards the vein centre, reflecting distinct but generally symmetric events (Fig. 3). Elemental mapping of an ocean crustal vein (Fig. 3d; Fig. S2) illuminates these multiple precipitation events with contrasting Sr concentrations in discrete calcium carbonate and clay domains composed of at least 4 distinct, broadly symmetrical, growth episodes. Vein microstructures also show evidence of multiple fracturing episodes through heterogenous crack localization away from the vein centre, incorporation of wall rock into the vein assemblage itself, and offsets relative to primary igneous minerals (Fig. 3). Many of these multiple

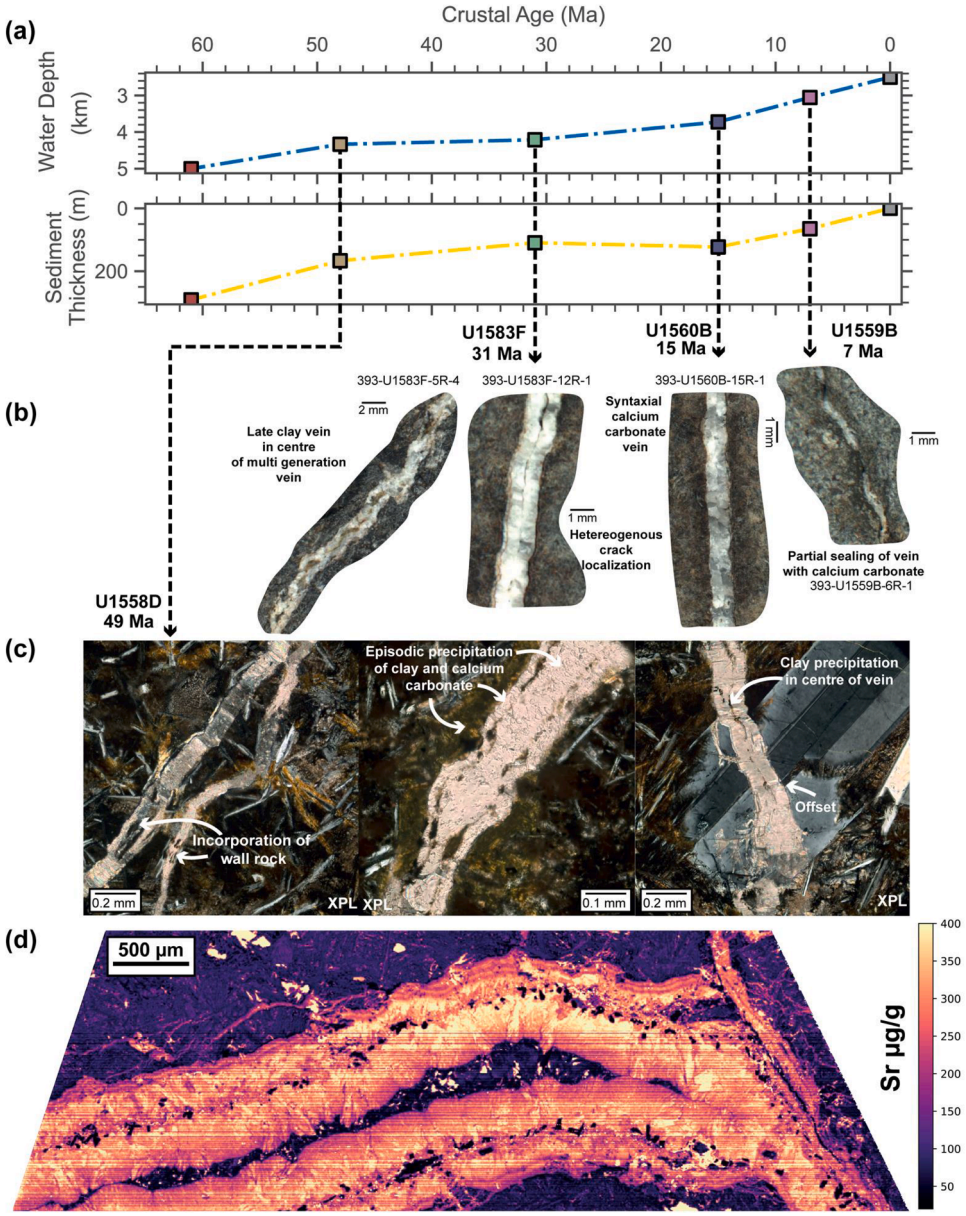

Fig. 3. (a) Water depth and sediment thickness of South Atlantic Transect (SAT) sites plotted against crustal age. (b) Whole-round core images acquired using DMT CoreScan3 (Grant et al., 2024) and (c) thin section photomicrographs of ocean crustal veins from the SAT showing macroscopic vein textures of multiple precipitation events and evidence of multiple cracking episodes. (d) Sr concentration (µg/g) relative differences are colour mapped accordingly using a linear colour map scale. Elemental mapping of an ocean crustal vein illuminates these multiple precipitation events (>4) with contrasting Sr concentrations in discrete calcium carbonate and clay domains. In the mapped region, some precipitation episodes show evidence of growth into open space and the incomplete sealing of the distinct event within the vein, where subsequent precipitation of low Sr calcium carbonate has filled the previously partially sealed vein centre.

event veins are polymineralic and display the alternating precipitation of different minerals (Fig. 3)

A compilation of veins logged during the South Atlantic Transect and at other IODP and ODP sites that meet the same vein logging criteria as SAT holes (all macroscopically visible veins logged) reveals that vein width distributions broaden with increasing crustal age (Fig. 4a; Fig. S3). For example, the 3.6 Ma Hole U1362A on the eastern flank of the Juan de Fuca Ridge yields a median vein width of 0.1 + 1 mm (2σ-equivalent; n = 1217), whereas the 167 Ma ODP Hole 801C on the western Pacific plate yields a median vein width of $0.3\pm^{4}_{0.1}$mm (2σ-equivalent; n = 3901) (Fig. 3a; Table 1). Both median vein width (Fig. 5a) and mean vein width (Fig. 5b) display relatively strong correlations with crustal age (R^2 = 0.5 and R^2 = 0.75, respectively). Maximum vein width increases with crustal age along the SAT from 3 mm in 7 Ma old crust to 30 mm in 61 Ma old crust (Fig. 4a; Table 1). In contrast, vein density ($\#_{veins}/m_{core}$; veins/m of recovered core) remains remarkably uniform across the aging ridge-flank, with median vein densities generally within 1σ for all crustal ages (Fig. 4b) and no correlation with crustal age (R^2 = 0.01, Fig. 5c). However, measured strain % ($(\Sigma m_{veins}/m_{core})\cdot 100$), where Σm_{veins} is the sum of vein widths (in m) and m_{core} is recovered core length (in m), progressively increases with crustal age (Fig. 4c), with a strong correlation (R^2 = 0.6; Fig. 5d). The average width per vein per metre of core $\left(\Sigma mm_{veins}/\frac{\#_{veins}}{m_{core}}\right)$, where Σmm_{veins} is the sum of vein widths (in mm) and $\frac{\#_{veins}}{m_{core}}$ is the vein density (veins/m) on a core-by-core basis, is also strongly correlated with crustal age (R^2 = 0.7; Fig. 5e; Fig. 4d). Together, these observations show that the width of upper ocean crustal veins progressively increases with crustal age, but vein densities remain uniform. This indicates that new fractures are not created as the crust ages. Consequently, this suggests that thicker veins in older sites are either the product of reactivation of pre-existing veins resulting in multiple precipitation episodes within the same vein, or reflect enhanced precipitation of vein material, or an interplay between both mechanisms.

4. Ocean plate-cooling-induced cracking

Taken together, vein microstructure observations, high resolution elemental mapping, and the progressively broadening of vein width distributions with crustal age but an approximately constant vein density across the South Atlantic Transect, indicate that some veins undergo multiple episodes of fracturing and precipitation indicating the transient presence of interconnected fluid pathways.

The similarity in vein densities at differing sites (Fig. 4; Fig. 5), irrespective of spreading rate and crustal age (Table 1; Fig. 1), are consistent with previous models of tectonic extensional accommodation, where extension is accommodated through ocean crustal faulting (e.g., Escartín et al., 1999; Estep et al., 2021; Olive et al., 2024) rather than core-scale fractures within individual lava flows. Consequently, variations in tectonic contributions to accretion typically do not affect upper ocean crust core-scale fractures and veins.

Previous models of ocean crustal crack filling propose fractures are initiated primarily due to cooling induced cracking during volcanic emplacement at the spreading ridge (Agar, 1990; Browning et al., 2016; Gillis and Sapp, 1997; Turcotte and Oxburgh, 1973) and are

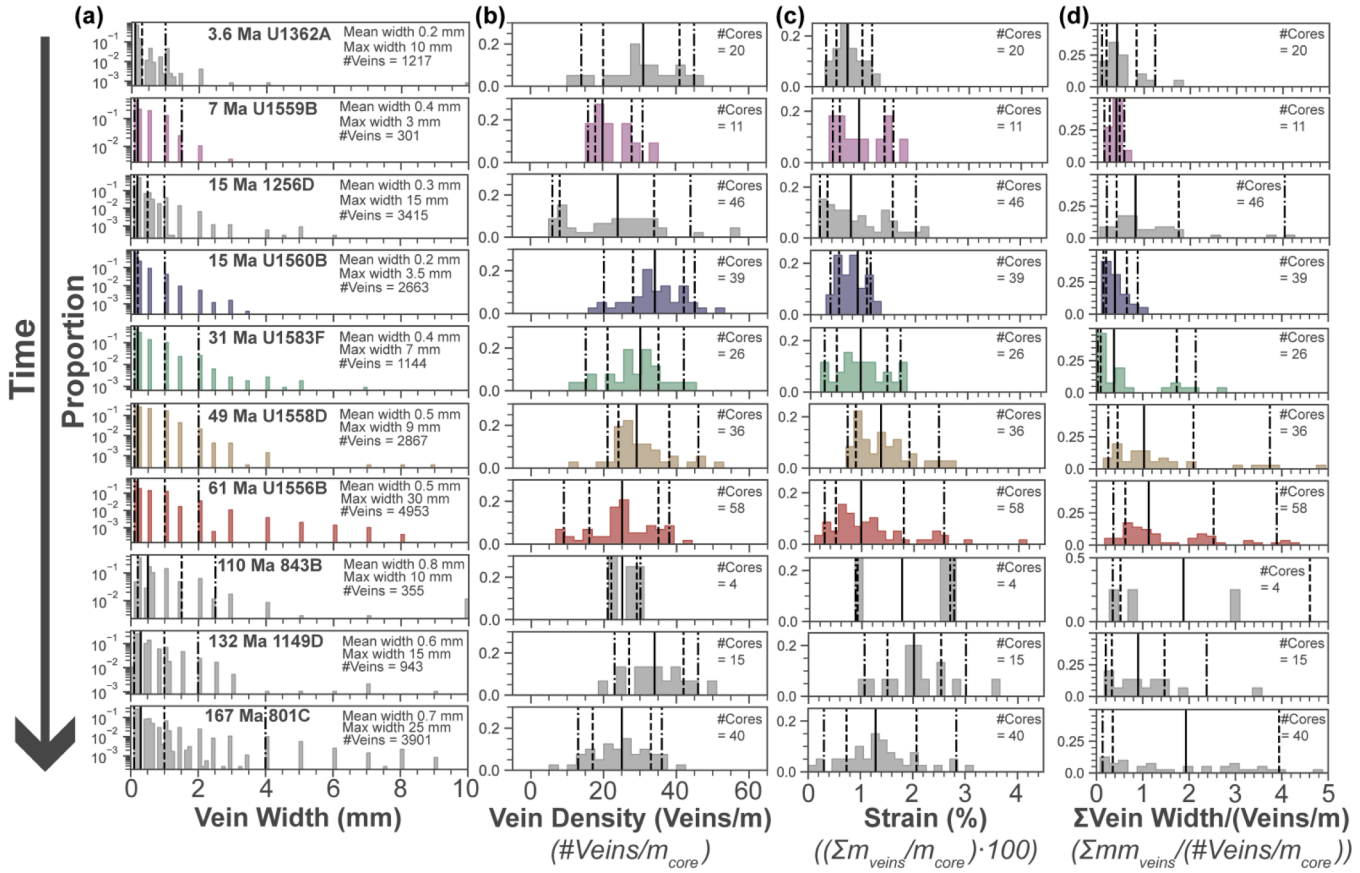

Fig. 4. (a) Vein width histograms of compiled scientific ocean drilling sites. We note that vein widths at each site are broadly consistent with a geometric distribution. (b) Vein density (number of veins per metre of recovered core; $\#_{veins}/m_{core}$) histograms on a core-by-core basis. (c) Strain (%) (metres of vein width / recovered core length; $\left(\frac{\Sigma m_{veins}}{m_{core}}\right)\cdot 100$) histograms on a core-by-core basis. (d) Average vein width (sum of vein widths/ veins per metre; $\Sigma mm_{veins}/\frac{\#_{veins}}{m_{core}}$) histograms on a core-by-core basis. Black lines show the median of the distribution with dashed lines equivalent to 1σ and dashdotted lines equivalent to 2σ.

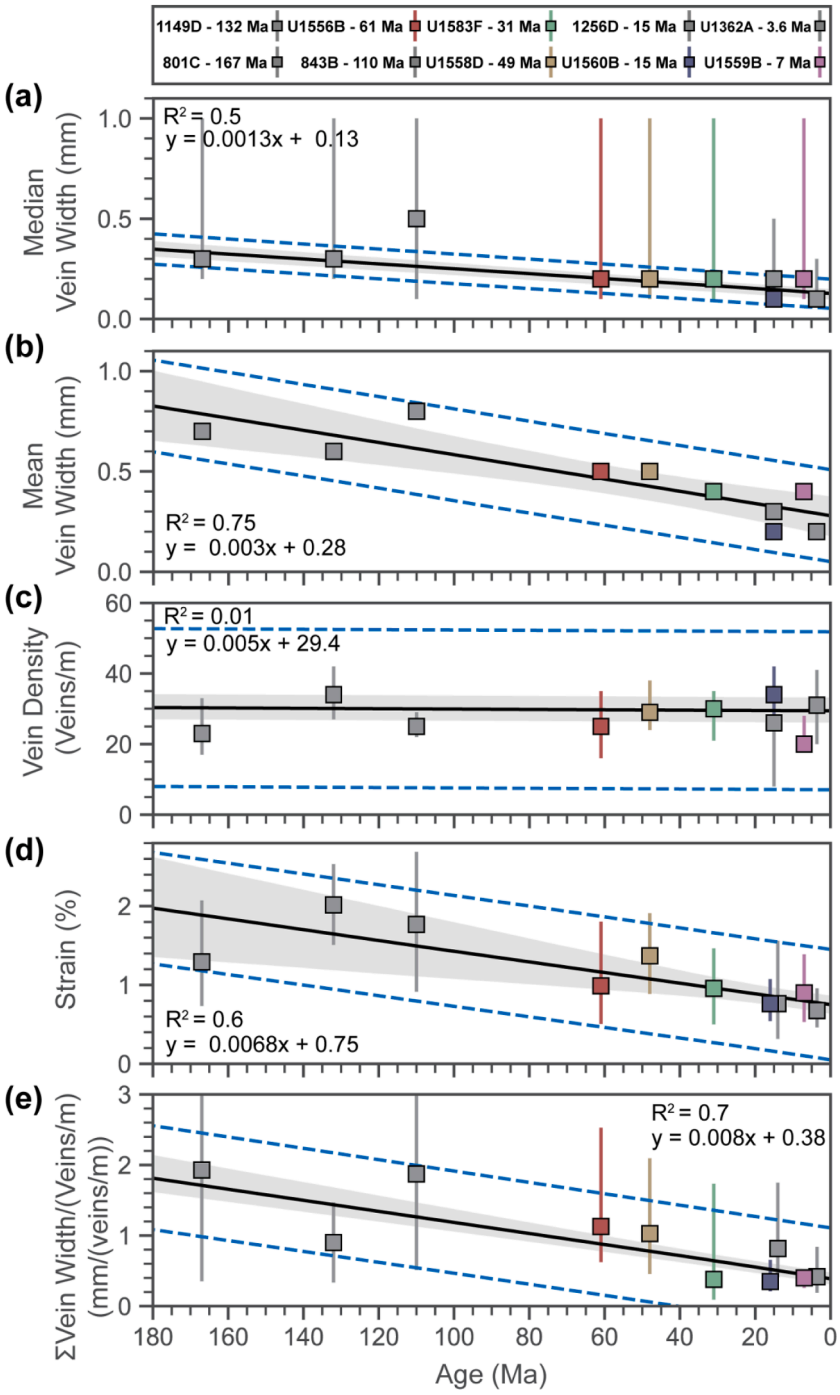

Fig. 5. (a) Median vein width of each site plotted against crustal age. (b) Mean vein width of each site plotted against crustal age. (c) Median vein density ($\#_{veins}\,/m_{core}$) plotted against crustal age with median values derived from the distribution of vein densities calculated from drilled cores at each site. (d) Median strain % ($(\Sigma m_{veins}\,/m_{core})\cdot 100$) plotted against crustal age with median values derived from the distribution of strain % calculated from drilled cores at each site. (e) Median value of the average vein width of a vein per core $\left(\Sigma \mathrm{mm}_{veins}\,/\frac{\#_{veins}}{m_{core}}\right)$ at each site plotted against crustal age with median values derived from the distribution that is calculated from drilled cores at each site. All error bars are equivalent to 1σ of the distribution. Histogram plots in Fig. 4 show the respective distributions. Black lines show the median Bayesian regression with grey shading reflecting the 95% confidence interval of the Bayesian regression and the blue dashed line showing the prediction band. Robust linear regression analysis was undertaken by leveraging a nested sampling Bayesian inversion engine termed UltraNest (Evans et al., 2024; Buchner, 2021). This approach implements a Monte Carlo technique Nested Sampling (Skilling, 2004) that provides parameter-based constraints of the data by exploring parameter space by applying Bayesian inference on prior probability distributions and in consequence generates posterior probability distributions (Evans et al., 2024; Buchner, 2021). R^2 values are derived from an ordinary least squares linear regression model.

progressively filled by precipitation of low temperature hydrothermal minerals from seawater-derived fluids passively circulating through the ridge flanks (Anderson et al., 1977; Jacobson, 1992; Stein and Stein, 1994). Our data challenge the notion that ocean crustal veins are passively filled and instead suggests they are dynamic features of ocean crust aging. Such a model is consistent with previous observations of recovered upper ocean crust drill core that display multiple fracturing and precipitation episodes within the same vein (Alt, 2004; Alt and Teagle, 1999, 2003; Dilek, 1998; Tartarotti et al., 1996). An explanation of how veins are progressively reactivated requires mechanisms that can produce a similar amount of strain to that observed in recovered ocean crustal drill cores (Fig. 4c), whilst also reconciling heat flow, seismic velocity data, and radiometric dating chronometry (Fig. 2).

Thermal stresses are inferred to be the primary source of stress that induces intra-plate seismicity and their reduction as the plate cools is invoked to explain the decrease in intra-plate seismicity with increasing plate age (Wiens and Stein, 1985). On-going cracking in the ocean lithosphere is inferred from recent ocean bottom seismometer observations around DSDP Hole 504B on ~7 Ma crust on the southern flank of the Costa Rica Rift (Tary et al., 2021). Microseismicity occurs from the seabed to depths of 15 to 20 km and is postulated to be caused by thermal stresses resulting from the non-uniform contraction of the cooling ocean plate (Tary et al., 2021), consistent with previous inferences of the magnitude and source of stress in ocean crust (Moos and Zoback, 1990).

Here we explore whether thermal contraction can generate sufficient strain to be invoked as a mechanism for ridge flank vein reactivation. As the ocean plate ages and traverses the ocean basin, it continues to cool and increases in density, inducing isostatic subsidence that deepens oceans (McKenzie, 1967; Parsons and Sclater, 1977; Stein and Stein, 1992; Turcotte and Oxburgh, 1967). Such quantitative ocean plate cooling models, ultimately derived from general seafloor topography, explicitly necessitate that the ocean lithosphere contracts with increasing age (Kumar and Gordon, 2009). We estimate the cumulative thermal strain derived from thermal contraction of the cooling ocean plate, following the cooling rate calculation approach of previous studies (Kumar and Gordon, 2009). We apply a half-space cooling model (Turcotte and Oxburgh, 1967) (Eq. 1) where T is temperature and is calculated following:

$$T(z,t) = T_m \cdot erfc\left[\frac{z}{2\sqrt{kt}}\right] \quad (1)$$

Where t is time, z is depth, T_m is the initial temperature, k is thermal diffusivity and erfc is the inverse error function. We average our calculations over a range of temperature and depth. Our approach is applied to the uniform contraction of the lithosphere and does not account for non-uniform contraction. We assume that the base of the competent lithosphere and seismogenic zone broadly follows the 600 °C isotherm (T_l) (Kumar and Gordon, 2009; McKenzie et al., 2005). Cooling-induced contraction is assumed to be a response to thermal stress averaged across the lithosphere, from the surface to the base of the 600 °C isotherm (Kumar and Gordon, 2009; Parmentier and Haxby, 1986). Although ocean crust contracts during crustal formation and emplacement of lavas, thermal contraction deeper in the ocean lithosphere persists. Consequently, thermal stresses are relieved by deformation through thermal strain contraction (Kumar and Gordon, 2009), resulting in the lower competent lithosphere in tension and the upper competent lithosphere in compression, as demonstrated by ocean earthquake focal mechanisms (Wessel, 1992; Wiens and Stein, 1985, 1983). Thus, we rearrange Eq. 1 so that l(t), the thickness of the competent lithosphere at time t, (Fig. S4a) is calculated by Eq. 2 (Collette, 1974; Kumar and Gordon, 2009; Wessel, 1992):

$$l(t) = 2\sqrt{kt} \cdot erfc^{-1} \cdot \left(\frac{T_l}{T_m}\right) \quad (2)$$

The depth averaged cooling rate of a competent lithosphere bounded by an isotherm (T_l) is calculated following Eq. 3 (Fig. S4b) (Kumar and Gordon, 2009):

$$\left(\frac{1}{l}\right)\int_0^l \left(\frac{\partial T}{\partial t}\right) dz = \frac{T_m \cdot \left[exp\left(-erfc^{-1}\left(\frac{T_l}{T_m}\right)^2\right) - 1\right]}{\left(2 \cdot \left(erfc^{-1}\left(\frac{T_l}{T_m}\right)\right) \cdot t \cdot \sqrt{\pi}\right)} \quad (3)$$

Thermal strain is calculated from the change in temperature (ΔT) (Fig. S4c) by multiplying by the coefficient of thermal expansion (α) following Eq. 4 (Fig. S4d):

$$\varepsilon = \alpha \cdot \Delta T \quad (4)$$

We estimate the underlying uncertainty of our strain model by applying a parameter bootstrapping approach assuming a uniform prior distribution (Table S3). We iterate the strain model 100,000 times to produce a posterior probability distribution of thermal strain. The model parameters empirically fitted to our core observations are consistent with previous studies (Haxby and Parmentier, 1988; Kumar and Gordon, 2009; McKenzie et al., 2005; McKenzie, 1967; Parmentier and Haxby, 1986; Stein and Stein, 1994, 1992; Turcotte and Oxburgh, 1967).

Our calculations of the depth averaged cumulative change in temperature with age (Fig. 6a) demonstrate that the rate of cooling significantly slows after ~65 million years. The corresponding cumulative thermal strain (accommodated by thermal contraction) model is empirically fitted to our core strain observations (Fig. 6b; Table S3) using geologically reasonable parameters consistent with previous studies (Kumar and Gordon, 2009; McKenzie et al., 2005; Wessel, 1992; Wessel and Haxby, 1990). The model demonstrates agreement with core observations, although some sites show a misfit between observed and modelled strain values, particularly those in older (Cretaceous and Jurassic) crust (Fig. 6b). Once the initial cooling-induced fracture network has been established during emplacement and cooling of the lavas, we propose that thermal contraction of the cooling ocean plate is the primary mechanism for the reopening of veins in ocean crust as it spreads away from mid-ocean ridges.

5. Duration of cracking and sealing

Ocean crust generated at fast-spreading rates in the Pacific and slow-spreading crust in the Atlantic yield contrasting conductive heat flow trends with crustal age (Fig. 2a; Fig. S5; Fig. S6). These differing heat flow trajectories are likely the result of contrasting volcanic architectures (Teagle et al., 2023). The greater basement topography inherited from more pronounced rifting at slower spreading ocean ridges of the Atlantic results in common occurrence of thinly sedimented or sediment-free basement highs being more common relative to the Pacific (Macdonald, 1982; Perfit and Chadwick, 2013), through which recharge and discharge hydrothermal fluid flows (Wheat and Fisher, 2008). Despite these contrasting spreading rate-induced seafloor bathymetries, the average hydrothermal heat flow anomaly persists for a similar time interval in both oceans (Fig. 2a). It has previously been postulated that a common thermal sealing mechanism is required to explain the similarity in the average hydrothermal sealing age (65 to 80 Ma; Fig. 2a) of both oceans (Stein and Stein, 1994).

Numerical simulations suggest that fractures in upper ocean crust play a key role in maintaining hydrothermal circulation and advective heat loss (Yang et al., 1996). There is a strong correlation ($R^2 = 0.99$; Fig. 7a) between the rate of change of the hydrothermal heat flux (TW/Myr) (Stein and Stein, 1994) and the strain rate (%/Myr) due to thermal contraction. We interpret this correlation as showing that thermal contraction of the cooling ocean plate provides a control on the duration of the hydrothermal heat flow anomaly, rather than the duration reflecting on-going passive sealing of the crust by precipitation of hydrothermal minerals (Anderson et al., 1977; Jacobson, 1992; Stein

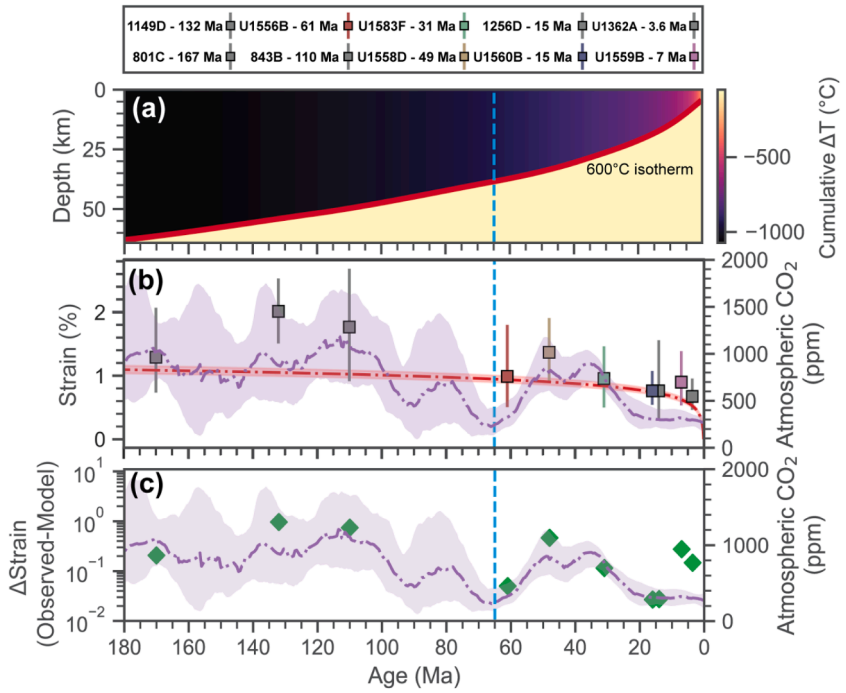

Fig. 6. (a) Ocean plate cooling model showing the depth averaged cumulative change in temperature (°C) against time. Depth is averaged from the 600 °C to 0 °C isotherm. The relative difference of the cumulative temperature change is colour mapped using a linear colour scale. Red line denotes the base of the seismogenic zone, assumed here to be the 600 °C isotherm. (b) Observed strain (%) calculated by a core-by-core basis plotted against age (Ma), at each site, squares reflect median strain (%) values of recovered cores $\left(\left(\frac{\Sigma m_{veins}}{m_{core}}\right)\cdot 100\right)$ with error bars showing variability within the distribution equivalent to 1σ. The dashdotted red line shows the median cumulative thermal strain value (ε) derived from parameter bootstrapped cooling ocean plate thermal strain model (see supplementary materials). Median atmospheric CO_2 (ppm) values (Foster et al., 2017) (dashdotted purple line) are also plotted against time with shading equivalent to 2σ. (c) Difference between the observed and modelled strain (i.e., model misfit) shown as green diamonds ($\Sigma m_{veins}/m_{core} - \varepsilon$). Error bars show variability within the distribution equivalent to 1σ. Median atmospheric CO_2 (ppm) values (Foster et al., 2017) (dashdotted purple line) are also plotted against time with shading equivalent to 2σ. We note that ΔStrain (Observed-Model) values in young sites (U1362A, U1559B) are higher than expected, likely due to logging of sub <0.1 mm veins as 0.1 mm veins (see methods for detail). Dashed blue line shows the global average age of thermal sealing of ocean crust (65 Ma; Stein and Stein, 1994).

and Stein, 1994). The reduction in the amount of strain produced by thermal contraction results in a slowing of the rate of cracking with age. The strong correlation between the rates of change in strain and hydrothermal heat flux indicates that the duration of fluid flow and advective heat loss in ocean crust is directly related to the ability of the system to reactivate existing veins. After ~>65 million years, low cracking rates mean that there is no rejuvenation of fluid pathways, ultimately resulting in the termination of the global average hydrothermal anomaly and the thermal 'sealing' of the ocean crust.

Although localized hydrothermal fluid flow can occur in crust of any age (Fig. 2a; Coggon et al., 2024a, 2022; Jarrard et al., 2003; Teagle et al., 2023), a model of continued cracking and sealing demonstrates how the cooling of the ocean plate itself drives a positive feedback mechanism in which cooling of the oceanic plate induces prolonged crustal cracking that ultimately results in advective heat loss and further cooling of the oceanic lithosphere. Such a model explains why observed upper ocean crustal seismic velocities change relatively rapidly (Fig. 2), but the global average hydrothermal anomaly persists for ~65 Myr and radiometric dating of secondary minerals suggests fluid flow throughout the crack network for up to 60 Myr after crustal formation (Fig. 2; Coogan et al., 2016; Hart and Staudigel, 1986; Kendrick et al., 2022; Laureijs et al., 2021). As the initial crack network is filled and seismic velocities mature (Anderson et al., 1977; Carlson, 2014; Stein and Stein, 1994), reactivation generates additional transient open space and permeability pathways that enable advective heat loss but these become filled by precipitation from ridge-flank hydrothermal fluids. This results in prolonged fluid flow and exchange between seawater-derived ridge-flank hydrothermal fluids and the upper oceanic crust that endures for tens of million years.

6. Changing global conditions

The mechanism of cracking and sealing alone fails to explain the misfit between measured and expected strain in drill cores (Fig. 6), so here we investigate the role of changing ocean chemistry on vein material abundance using past ocean chemistry based on reconstructions of atmospheric CO_2 concentrations (Foster et al., 2017; Zeebe, 2012). A strong linear correlation ($R^2 = 0.5$) between atmospheric CO_2 at the age of crustal formation and ΔStrain (Observed-Model; $\Sigma m_{veins}/m_{core} - \varepsilon$) (Fig. 7) suggests that a warmer, high CO_2, world results in greater vein material volumetric abundance, as proposed by previous studies (Alt and Teagle, 1999; Gillis and Coogan, 2011). Consequently, the discrepancy between measured and expected strain (defined as ΔStrain Observed-Model; $\Sigma m_{veins}/m_{core} - \varepsilon$) can be reconciled by considering changing global conditions as a mechanism controlling excess vein material abundance. We propose that the amount of excess vein material at each site that cannot be explained by prolonged cracking and sealing, is related to distinct ocean chemistry at the time of crustal formation.

Such a mechanism is consistent with published radiometric dating of secondary minerals (Fig. 2c). Dating of calcium carbonate veins from Cretaceous and Jurassic high CO_2 worlds (Fig. 6) suggests formation within error of crustal formation (Fig. 2c) (Coogan et al., 2016; Kendrick et al., 2022). This indicates that an additional strain component in a vein at a given site results from early precipitation of hydrothermal minerals, infilling interconnected porosity derived from the initial cooling and emplacement of seafloor lavas during accretion. After the early formation of vein material, some interconnected porosity in fractures is likely closed due to overburden of the water and sediment column, and compression due to ocean lithosphere unbending away from mid-ocean

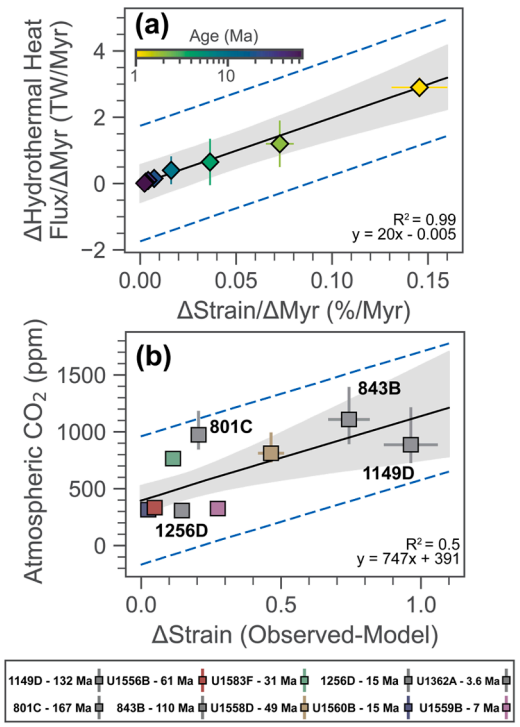

Fig. 7. (a) Rate of change of the global average hydrothermal heat flux (1 to 65 Ma; Stein and Stein, 1994) plotted against strain rate (%/Myr) from the ocean plate cooling model of this study. Crustal age of each point is shown with a logarithmic colour map. Data are provided in Table S15. (b) Atmospheric CO_2 plotted against the difference between observed strain from recovered scientific ocean drilling cores and modelled thermal strain ($\Sigma m_{veins}/m_{core} - \varepsilon$). Black lines show the median Bayesian regression with grey shading reflecting the 95% confidence interval of the Bayesian regression and the blue dashed line showing the prediction band. R^2 values are derived from an ordinary least squares linear regression model.

ridge axial relief (Olive et al., 2024). During subsequent crustal aging, veins are reactivated by the cooling of the ocean plate, resulting in veins wider than expected from cracking and sealing exclusively, as their widths reflect contributions from both mechanisms. In contrast, in colder low CO_2 worlds, early precipitation of hydrothermal minerals is less extensive, resulting in veins without significant excess strain components (i.e., negligible ΔStrain Observed-Model; Fig. 7b). Hence, the majority of their observed strain is derived from progressive cracking and sealing, induced by thermal contraction.

The implication of this simple relationship between vein width and crustal age is that a positive feedback occurs between cooling of the ocean plate and the abundance of secondary minerals hosted in veins. Our analysis shows that progressive cracking and sealing alone cannot explain vein observations from recovered cores. As the abundance of additional vein material strongly correlates with ocean chemistry, we conclude that hydrothermal veins record a dynamic interplay between the age of ocean crust, changing ocean conditions, and cooling of the ocean plate, with their relative contributions varying throughout geological time, dependent on global conditions. Despite this variation, our data indicate that the upper ocean crust endures as an active geochemical reservoir, contributing to global biogeochemical cycles for tens of million years (up to ~80 Myr; Fig. 2) after its formation.

CRediT authorship contribution statement

Aled D. Evans: Conceptualization, Data curation, Formal analysis, Funding acquisition, Investigation, Methodology, Project administration, Software, Validation, Visualization, Writing – original draft, Writing – review & editing. **Rosalind M. Coggon:** Writing – review & editing, Validation, Methodology, Investigation, Funding acquisition, Conceptualization. **Michelle Harris:** Writing – review & editing, Methodology, Investigation. **Elliot J. Carter:** Writing – review & editing, Methodology, Investigation. **Elmar Albers:** Writing – review & editing, Methodology, Investigation. **Gilles M. Guérin:** Writing – review & editing, Visualization, Investigation. **Thomas M. Belgrano:** Writing – review & editing, Methodology, Investigation. **Mallika Jonnalagadda:** Writing – review & editing, Methodology, Investigation. **Lewis J.C. Grant:** Writing – review & editing, Methodology, Investigation. **Pamela D. Kempton:** Writing – review & editing, Methodology, Investigation. **David J. Sanderson:** Writing – review & editing, Validation, Conceptualization. **James A. Milton:** Writing – review & editing, Methodology, Investigation. **Timothy J. Henstock:** Writing – review & editing, Validation, Methodology. **Jeff C. Alt:** Investigation, Methodology, Writing – review & editing. **Damon A.H. Teagle:** Writing – review & editing, Methodology, Investigation, Funding acquisition, Conceptualization.

Declaration of competing interest

The authors declare that they have no known competing financial interests or personal relationships that could have appeared to influence the work reported in this paper.

Acknowledgements

The cores and data used in this study were provided by the International Ocean Discovery Program (IODP). We thank: JOIDES Resolution Captains Harm Nienhuis, Jake Robinson and Tom Haart; Operations Superintendents Steve Midgley, Bill Rhinehart and Kevin Grigar; Offshore Installation Managers Wayne Lambert and Mark Robinson; and the entire SIEM Offshore JOIDES Resolution crew and staff and the Texas A&M University technical staff onboard IODP South Atlantic Transect Expeditions 390C, 395E, 390 and 393. We thank the JOIDES Resolution Science Operator for implementing Engineering Expeditions 390C and 395E during the pandemic, when international travel restrictions prevented scientists sailing, and the technical staff of Expeditions 390C and 395E led by Chieh Peng, Aaron de Loach and Beth Novak for their efforts curating and analyzing cores during the engineering expeditions. We thank the science party members of Expedition 390 and 393 and expedition project managers Emily Estes and Trevor Williams. ADE acknowledges a UKRI NERC UK IODP Moratorium award (NE/X00631X/1), awarded to ADE and DAHT, and a Royal Society URF awarded to RMC (URF\R1\180320 and URF\R\231021). We also acknowledge UKRI NERC UK IODP Moratorium awards to RMC (NE/X0001X/1); DAHT (NE/X009440/1); LJCG, RMC, DAHT (NE/X002446/1); and TMB and DAHT (NE/X003485/1). We thank Stephen Roberts for conversations on vein networks. We also thank Dan Doran and Matthew Beverly-Smith for the preparation of thick sections. We thank Carolina Lithgow-Bertelloni for editorial handing and two anonymous reviewers for their constructive reviews that improved this paper.

Supplementary materials

Supplementary material associated with this article can be found, in the online version, at doi:10.1016/j.epsl.2024.119116.

Data availability

All data used in this study are provided in the supplementary materials or are cited accordingly.

References

Agar, S.M., 1990. Fracture evolution in the upper ocean crust: evidence from DSDP hole 504B. Geol. Soc. Spec. Publ. 54, 41–50.

Albers, E., Jöns, S., Gerdes, A., Klügel, A., Beier, C., Kasemann, S.A., Bach, W., 2023. Timing of carbon uptake by oceanic crust determined by rock reactivity. Geology 51 (9), 875–879. https://doi.org/10.1130/G51238.1.

Alt, J.C., Teagle, D.A.H., 1999. The uptake of carbon during alteration of ocean crust. Geochim. Cosmochim. Acta 63, 1527–1535.

Alt, J.C., Teagle, D.A.H., 2003. Hydrothermal alteration of upper oceanic crust formed at a fast-spreading ridge: mineral, chemical, and isotopic evidence from ODP Site 801. Chem. Geol. 201, 191–211.

Alt, J.C., Teagle, D.A.H., Laverne, C., Vanko, D.A., Bach, W., Honnorez, J., Becker, K., Ayadi, M., Pezard, P.A., 1996. Ridge flank alteration of upper ocean crust in the eastern pacific: synthesis of results for volcanic rocks of holes 504B and 896A1. In: Proceedings of the ocean drilling program, scientific results. researchgate.net, pp. 435–450.

Alt, J.C., Laverne, C., Coggon, R.M., Teagle, D.A.H., Banerjee, N.R., Morgan, S., Smith-Duque, C.E., Harris, M., Galli, L., 2010. Subsurface structure of a submarine hydrothermal system in ocean crust formed at the east pacific rise, ODP/IODP Site 1256. Geochemistry, geophysics, geosystems 11. https://doi.org/10.1029/2010GC003144.

Alt, J.C., 2004. Alteration of the upper oceanic crust: mineralogy, chemistry, and processes. Hydrogeol. Ocean. Lithosph. 1, 495. –433.

Anderson, R.N., Langseth, M.G., Sclater, J.G., 1977. The mechanisms of heat transfer through the floor of the Indian Ocean. J. Geophys. Res. 82, 3391–3409.

Bach, W., Edwards, K.J., 2003. Iron and sulfide oxidation within the basaltic ocean crust: implications for chemolithoautotrophic microbial biomass production. Geochim. Cosmochim. Acta 67, 3871–3887.

Berner, R.A., Berner, E.K., 1997. Silicate weathering and climate. In: Ruddiman, W.F. (Ed.), Tectonic uplift and climate change. Springer US, Boston, MA, pp. 353–365.

Berner, R.A., Lasaga, A.C., Garrels, R.M., 1983. The carbonate-silicate geochemical cycle and its effect on atmospheric carbon dioxide over the past 100 million years. Am. J. Sci. 283, 641–683.

Bons, P.D., Elburg, M.A., Gomez-Rivas, E., 2012. A review of the formation of tectonic veins and their microstructures. J. Struct. Geol. 43, 33–62.

Grant, L.J.C., Evans, A.D., Coggon, R.M., Estep, J.D., McIntyre, A., Slagle, A., Widlansky, S.J., Albers, E., Harris, M., Teagle, D.A.H., Sylvan, J.B., Reece, J.S., and the Expedition 390/393 Scientists, 2024. Data report: high-resolution digital imaging of whole-round hard rocks collected during IODP Expeditions 390C, 395E, 390, and 393, South Atlantic Transect, using a DMT CoreScan3. In Coggon, R.M., Teagle, D.A.H., Sylvan, J.B., Reece, J., Estes, E.R., Williams, T.J., Christeson, G.L., and the Expedition 390/393 Scientists, South Atlantic Transect. Proceedings of the International Ocean Discovery Program, 390/393: College Station, TX (International Ocean Discovery Program). https://doi.org/10.14379/iodp.proc.390393.209.2024.

Browning, J., Meredith, P., Gudmundsson, A., 2016. Cooling-dominated cracking in thermally stressed volcanic rocks. Geophys. Res. Lett. 43, 8417–8425.

Buchner, J., 2021. UltraNest–a robust, general purpose Bayesian inference engine. arXiv preprint arXiv:2101.09604.

Carlson, R.L., 2014. The influence of porosity and crack morphology on seismic velocity and permeability in the upper oceanic crust. Geochem. Geophys. Geosyst. 15, 10–27.

Christeson, G.L., Goff, J.A., Reece, R.S., 2019. Synthesis of oceanic crustal structure from two-dimensional seismic profiles. Rev. Geophys. 57, 504–529.

Cleveland, W.S., 1979. Robust Locally Weighted Regression and Smoothing Scatterplots. J. Am. Stat. Assoc. 74, 829–836.

Coggon, R.M., Teagle, D.A.H., 2011. Hydrothermal calcium-carbonate veins reveal past ocean chemistry. Trends Analyt. Chem. 30, 1252–1268.

Coggon, R.M., Teagle, D.A.H, Cooper, M.J., Vanko, D.A., 2004. Linking basement carbonate vein compositions to porewater geochemistry across the eastern flank of the Juan de Fuca Ridge, ODP Leg 168. Earth Planet. Sci. Lett. 219 (1–2), 111–128.

Coggon, R.M., Teagle, D.A.H., Harris, M., Davidson, G.J., 2016. Hydrothermal contributions to global biogeochemical cycles: Insights from the Macquarie Island ophiolite. Lithos.

Coggon, R.M., Teagle, D.A.H., Harris, M., Davidson, G.J., Alt, J.C., Brewer, T.S., 2016. Hydrothermal contributions to global biogeochemical cycles: Insights from the Macquarie Island ophiolite. Lithos 264, 329–347.

Coggon, R.M., Sylvan, J.B., Teagle, D.A.H., Reece, J., Christeson, G.L., Estes, E.R., Williams, T.J., 2022. and the Expedition 390 Scientists, 2022. Expedition 390 Preliminary Report: South Atlantic Transect 1. International Ocean Discovery Program. https://doi.org/10.14379/iodp.pr.390.2022.

Coggon, R.M., Teagle, D.A.H., Sylvan, J.B., Reece, J., Estes, E.R., Williams, T.J., Christeson, G.L., Aizawa, M., Albers, E., Amadori, C., Belgrano, T.M., Borrelli, C., Bridges, J.D., Carter, E.J., D'Angelo, T., Dinares-Turell, J., Doi, N., Estep, J.D., Evans, A., Gilhooly, W.P., III, Grant, L.J.C., Guerin, G.M., Harris, M., Hojnacki, V.M., Hong, G., Jin, X., Jonnalagadda, M., Kaplan, M.R., Kempton, P.D., Kuwano, D., Labonte, J. M., Lam, A.R., Latas, M., Lowery, C.M., Lu, W., McIntyre, A., Moal-Darrigade, P., Pekar, S.F., Robustelli Test, C., Routledge, C.M., Ryan, J.G., Santiago Ramos, D., Shchepetkina, A., Slagle, A.L., Takada, M., Tamborrino, L., Villa, A., Wang, Y., Wee, S.Y., Widlansky, S.J., Yang, K., Kurz, W., Prakasam, M., Tian, L., Yu, T., and Zhang, G., 2024. Expedition 390/393 summary. In Coggon, R.M., Teagle, D.A.H., Sylvan, J. B., Reece, J., Estes, E.R., Williams, T.J., Christeson, G.L., and the Expedition 390/393 Scientists, South Atlantic Transect. Proceedings of the International Ocean Discovery Program, 390/393: College Station, TX (International Ocean Discovery Program). https://doi.org/10.14379/iodp.proc.390393.101.2024.

Coggon, R.M., Teagle, D.A.H., Sylvan, J.B., Reece, J., Estes, E.R., Williams, T.J., Christeson, G.L., Aizawa, M., Albers, E., Amadori, C., Belgrano, T.M., Borrelli, C., Bridges, J.D., Carter, E.J., D'Angelo, T., Dinares-Turell, J., Doi, N., Estep, J.D., Evans, A., Gilhooly, W.P., III, Grant, L.J.C., Guerin, G.M., Harris, M., Hojnacki, V.M., Hong, G., Jin, X., Jonnalagadda, M., Kaplan, M.R., Kempton, P.D., Kuwano, D., Labonte, J. M., Lam, A.R., Latas, M., Lowery, C.M., Lu, W., McIntyre, A., Moal-Darrigade, P., Pekar, S.F., Robustelli Test, C., Routledge, C.M., Ryan, J.G., Santiago Ramos, D., Shchepetkina, A., Slagle, A.L., Takada, M., Tamborrino, L., Villa, A., Wang, Y., Wee, S.Y., Widlansky, S.J., Yang, K., Kurz, W., Prakasam, M., Tian, L., Yu, T., and Zhang, G., 2024. Expedition 390/393 methods. In Coggon, R.M., Teagle, D.A.H., Sylvan, J. B., Reece, J., Estes, E.R., Williams, T.J., Christeson, G.L., and the Expedition 390/393 Scientists, South Atlantic Transect. Proceedings of the International Ocean Discovery Program, 390/393: College Station, TX (International Ocean Discovery Program). https://doi.org/10.14379/iodp.proc.390393.102.2024.

Collette, B.J., 1974. Thermal contraction joints in a spreading seafloor as origin of fracture zones. Nature 251, 299–300.

Coogan, L.A., Gillis, K.M., 2018. Low-temperature alteration of the seafloor: impacts on ocean chemistry. Annu. Rev. Earth Planet. Sci. 46, 21–45.

Coogan, L.A., Parrish, R.R., Roberts, N.M.W., 2016. Early hydrothermal carbon uptake by the upper oceanic crust: Insight from in situ U-Pb dating. Geology 44, 147–150.

Dilek, Y., 1998. Structure and tectonics of intermediate-spread oceanic crust drilled at DSDP/ODP Holes 504B and 896A, Costa Rica Rift. Geol. Soc. Spec. Publ. 131, 177–197.

Escartín, J., Cowie, P.A., Searle, R.C., Allerton, S., Mitchell, N.C., MacLeod, C.J., Slootweg, A.P., 1999. Quantifying tectonic strain and magmatic accretion at a slow spreading ridge segment, Mid-Atlantic Ridge, 29°N. J. Geophys. Res. 104, 10421–10437.

Estep, J., Reece, B., Christeson, G.L., Kardell, D.A., Carlson, R.L., 2021. 70 million years of seafloor spreading and magmatism in the South Atlantic. Earth Planet. Sci. Lett. 574, 117173.

Evans, A.D., Foster, G.L., Teagle, D.A.H., 2024. Constraining uncertainty in boron isotope systematics using a Bayesian inversion engine reveals contrasting parameter sensitivities. Chem. Geol. 648, 121953.

Expedition 327 Scientists, 2011. Site U1362. In: and the Expedition 327 Scientists, Proc. IODP, 327: Tokyo (Integrated Ocean Drilling Program Management International, Inc. https://doi.org/10.2204/iodp.proc.327.103.2011.

Fisher, A.T., Becker, K., 2000. Channelized fluid flow in oceanic crust reconciles heat-flow and permeability data. Nature 403 (6765), 71–74.

Foster, G.L., Royer, D.L., Lunt, D.J., 2017. Future climate forcing potentially without precedent in the last 420 million years. Nat. Commun. 8, 14845.

Fuchs, S., Norden, B., Artemieva, I., Chiozzi, P., Dedecek, P., Demezhko, D., Förster, A., Gola, G., Gosnold, W., Hamza, V., Harris, R., He, L., Huang, S., Kohl, T., Lee, Y., Liu, S., Podugu, N., Negrete-Aranda, R., Poort, J., Roy, S., Tanaka, A., Vakhitova, G., Verdoya, M., 2021. The Global Heat Flow Database: Release 2021. https://doi.org/10.5880/fidgeo.2021.014.

Gillis, K.M., Coogan, L.A., 2011. Secular variation in carbon uptake into the ocean crust. Earth Planet. Sci. Lett. 302, 385–392.

Gillis, K.M., Sapp, K., 1997. Distribution of porosity in a section of upper oceanic crust exposed in the Troodos Ophiolite. J. Geophys. Res. 102, 10133–10149.

Grevemeyer, I., Kaul, N., Villinger, H., Weigel, W., 1999. Hydrothermal activity and the evolution of the seismic properties of upper oceanic crust. J. Geophys. Res. 104, 5069–5079.

Hart, S.R., Staudigel, H., 1986. Ocean crust vein mineral deposition: Rb/Sr ages, U-Th-Pb geochemistry, and duration of circulation at DSDP sites 261, 462 and 516. Geochim. Cosmochim. Acta 50, 2751–2761.

Haxby, W.F., Parmentier, E.M., 1988. Thermal contraction and the state of stress in the oceanic lithosphere. J. Geophys. Res. 93, 6419.

Houtz, R., Ewing, J., 1976. Upper crustal structure as a function of plate age. J. Geophys. Res. 81, 2490–2498.

Jacobson, R.S., 1992. Impact of crustal evolution on changes of the seismic properties of the uppermost ocean crust. Rev. Geophys. 30, 23–42.

Jarrard, R.D., Abrams, L.J., Pockalny, R., Larson, R.L., Hirono, T., 2003. Physical properties of upper oceanic crust: Ocean Drilling Program Hole 801C and the waning of hydrothermal circulation. J. Geophys. Res. 108. https://doi.org/10.1029/2001jb001727.

Jochum, K.P., Nohl, U., Herwig, K., Lammel, E., Stoll, B., Hofmann, A.W., 2005. GeoReM: a new geochemical database for reference materials and isotopic standards. Geostand. Geoanal. Res. 29 (3), 333–338.

Kardell, D.A., Christeson, G.L., Estep, J.D., Reece, R.S., Carlson, R.L., 2019. Long-lasting evolution of layer 2A in the western south Atlantic: Evidence for low-temperature hydrothermal circulation in old oceanic crust. J. Geophys. Res. [Solid Earth] 124, 2252–2273.

Kendrick, M.A., Zhao, J., Feng, Y., 2022. Early accretion and prolonged carbonation of the Pacific Ocean's oldest crust. Geology 50 (11), 1270–1275.

Kumar, R.R., Gordon, R.G., 2009. Horizontal thermal contraction of oceanic lithosphere: The ultimate limit to the rigid plate approximation. J. Geophys. Res. 114. https://doi.org/10.1029/2007jb005473.

Laureijs, C.T., Coogan, L.A., Spence, J., 2021. In-situ Rb-Sr dating of celadonite from altered upper oceanic crust using laser ablation ICP-MS/MS. Chem. Geol. 579, 120339.

Li, S., Suo, Y., Yu, S., Wu, T., Somerville, I., Sager, W., Li, X., Hui, G., Zhang, Y., Zang, Y., Zheng, Q., 2016. Orientation of joints and arrangement of solid inclusions in fibrous veins in the Shatsky Rise, NW Pacific: implications for crack-seal mechanisms and stress fields. Geol. J. 51, 562–578.

Macdonald, K.C., 1982. Mid-ocean ridges: fine scale tectonic, volcanic and hydrothermal processes within the plate boundary zone. Annu. Rev. Earth Planet. Sci. 10, 155–190.

McKenzie, D.P., 1967. Some remarks on heat flow and gravity anomalies. J. Geophys. Res. 72 (24), 6261–6273.

McKenzie, D., Jackson, J., Priestley, K., 2005. Thermal structure of oceanic and continental lithosphere. Earth Planet. Sci. Lett. 233, 337–349.

Moos, D., Marion, D., 1994. Morphology of extrusive basalts and its relationship to seismic velocities in the shallow oceanic crust. J. Geophys. Res. 99, 2985–2994.

Moos, D., Zoback, M.D., 1990. Utilization of observations of well bore failure to constrain the orientation and magnitude of crustal stresses: Application to continental, Deep Sea Drilling Project, and Ocean Drilling Program boreholes. J. Geophys. Res. 95, 9305.
Olive, J.A., Ekström, G., Buck, W.R., Liu, Z., Escartín, J., Bickert, M., 2024. Mid-ocean ridge unfaulting revealed by magmatic intrusions. Nature 628, 782–787.
Parmentier, E.M., Haxby, W.F., 1986. Thermal stresses in the oceanic lithosphere: Evidence from geoid anomalies at fracture zones. J. Geophys. Res. 91, 7193–7204.
Parsons, B., Sclater, J.G., 1977. An analysis of the variation of ocean floor bathymetry and heat flow with age. J. Geophys. Res. 82, 803–827.
Paton, C., Hellstrom, J., Paul, B., Woodhead, J., Hergt, J., 2011. Iolite: Freeware for the visualisation and processing of mass spectrometric data. J. Anal. At. Spectrom. 26, 2508–2518.
Perfit, M., Chadwick, W., 2013. Magmatism at mid-ocean ridges: Constraints from volcanological and geochemical investigations. Geophys. Monogra. 106, 59–115.
Ramsay, J.G., 1980. The crack–seal mechanism of rock deformation. Nature 284, 135–139.
Reece, R., Estep, J., 2019. Processed MCS (PSTM) data from the Mid-Atlantic Ridge (MAR) to the Rio Grande Rise, South Atlantic Ocean, acquired by the R/V Marcus G. Langseth in 2016 (MGL1601).
Rohr, K.M.M., 1994. Increase of seismic velocities in upper oceanic crust and hydrothermal circulation in the Juan de Fuca plate. Geophys. Res. Lett. 21, 2163–2166.
Ryan, W.B.F., Carbotte, S.M., Coplan, J.O., O'Hara, S., Melkonian, A., Arko, R., Weissel, R.A., Ferrini, V., Goodwillie, A., Nitsche, F., Bonczkowski, J., Zemsky, R., 2009. Global multi-resolution topography synthesis: Global multi-resolution topography synthesis. Geochem. Geophys. Geosyst. 10. https://doi.org/10.1029/2008gc002332.
Seton, M., Müller, R.D., Zahirovic, S., Williams, S., Wright, N.M., Cannon, J., Whittaker, J.M., Matthews, K.J., McGirr, R., 2020. A global data set of present-day oceanic crustal age and seafloor spreading parameters. Geochem. Geophys. Geosyst. 21. https://doi.org/10.1029/2020gc009214.
Shipboard Scientific Party, 1992. Site 843. In: *Proc. ODP, Init. Repts.*, 136 Ocean Drilling Program, College Station, TX, pp. 65–99. https://doi.org/10.2973/odp.proc.ir.136.105.1992.
Shipboard Scientific Party, 2000. Site 801. Ocean Drilling Program, Repts., 185: College Station, TX, pp. 1–222. https://doi.org/10.2973/odp.proc.ir.185.103.2000.
Shipboard Scientific Party, 2000. Site 1149. Ocean Drilling Program, Repts., 185: College Station, TX, pp. 1–190. https://doi.org/10.2973/odp.proc.ir.185.104.2000.
Shipboard Scientific Party, 2003. Site 1256. In: *Proc. ODP, Init. Repts.*, 206 Ocean Drilling Program, College Station, TX, pp. 1–396. https://doi.org/10.2973/odp.proc.ir.206.103.2003.
Skilling, J., 2004. Nested Sampling. AIP Conf. Proc. 735, 395–405.
Stein, C.A., Stein, S., 1992. A model for the global variation in oceanic depth and heat flow with lithospheric age. Nature 359, 123–129.
Stein, C.A., Stein, S., 1994. Constraints on hydrothermal heat flux through the oceanic lithosphere from global heat flow. J. Geophys. Res. 99, 3081–3095.
Tartarotti, P., Vanko, D., Harper, G.D., Dilek, Y., 1996. 19. Crack-seal veins in upper layer 2 in Hole 896a1. Scient. Results 148, 281–288.
Tary, J.B., Hobbs, R.W., Peirce, C., Lesmes Lesmes, C., Funnell, M.J., 2021. Local rift and intraplate seismicity reveal shallow crustal fluid-related activity and sub-crustal faulting. Earth Planet. Sci. Lett. 562, 116857.
Teagle, D.A.H., Scientists, E.393, Reece, J., Coggon, R.M., Sylvan, J.B., Christeson, G.L., Williams, T.J., Estes, E.R., 2023. Expedition 393 Preliminary Report: South Atlantic Transect 2. International Ocean Discovery Program. https://doi.org/10.14379/iodp.pr.393.2023.
Turcotte, D.L., Oxburgh, E.R., 1967. Finite amplitude convective cells and continental drift. J. Fluid Mech. 28, 29–42.
Turcotte, D.L., Oxburgh, E.R., 1973. Mid-plate Tectonics. Nature 244, 337–339.
Wessel, P., Haxby, W.F., 1990. Thermal stresses, differential subsidence, and flexure at oceanic fracture zones. J. Geophys. Res. 95, 375–391.
Wessel, P., 1992. Thermal stresses and the bimodal distribution of elastic thickness estimates of the oceanic lithosphere. J. Geophys. Res. 97, 14177–14193.
Wheat, C.G., Fisher, A.T., 2008. Massive, low-temperature hydrothermal flow from a basaltic outcrop on 23 Ma seafloor of the Cocos Plate: Chemical constraints and implications. Geochem. Geophys. Geosyst. 9. https://doi.org/10.1029/2008gc002136.
Wiens, D.A. and Stein, S., 1983. Age dependence of oceanic intraplate seismicity and implications for lithospheric evolution. Journal of Geophysical Research: Solid Earth, 88(B8), pp.6455-6468.
Wiens, D.A., Stein, S., 1985. Implications of oceanic intraplate seismicity for plate stresses, driving forces and rheology. Tectonophysics 116, 143–162.
Wilkens, R.H., Fryer, G.J., Karsten, J., 1991. Evolution of porosity and seismic structure of upper oceanic crust: Importance of aspect ratios. J. Geophys. Res. 96, 17981.
Yang, J., Edwards, R.N., Molson, J.W., Sudicky, E.A., 1996. Fracture-induced hydrothermal convection in the oceanic crust and the interpretation of heat-flow data. Geophys. Res. Lett. 23, 929–932.
Zeebe, R.E., 2012. History of seawater carbonate chemistry, atmospheric CO2, and ocean acidification. Annu. Rev. Earth Planet. Sci. 40, 141–165.